Texture Modeling Using Contourlets and Finite Mixtures of Generalized Gaussian Distributions and Applications

Mohand Saïd Allili, *Member, IEEE*, Nadia Baaziz, *Member, IEEE*, and Marouene Mejri

***Abstract*—In this paper, we develop a new framework for contourlet-based statistical modeling using finite Mixtures of Generalized Gaussian distributions (MoGG). On the one hand, given the rich directional information provided by the contourlet transform (CT), we propose to use a redundant version of the CT, which describes texture structures more accurately. On the other hand, we use MoGG modeling of contourlet coefficients distribution, which allows for precise capturing of a wide range of histogram shapes and provides better description and discrimination of texture than single probability density functions (pdfs). Moreover, we propose three applications for the proposed approach, namely: (1) texture retrieval, (2) fabric texture defect detection, and 3) infrared (IR) face recognition. We compare two implementations of the CT: standard CT (SCT) and redundant CT (RCT). We show that the proposed approach yields better results in the applications studied compared to recent state-of-the-art methods.**

***Index Terms*—Fabric texture defect detection, IR face recognition, Mixture of Generalized Gaussian distributions (MoGG), standard/redundant contourlet transforms, texture retrieval.**

I. Introduction

TWO-DIMENSIONAL texture images contain geometrical structures with various scales and directional elements that play a fundamental role in its interpretation and understanding. Given the adequacy of the human visual perception to spatial-frequency representations of signals, significant effort has been put into applying multiscale image representations, such as wavelet transforms, as a means to help capture and exhibit image texture details and structures with space-frequency localization [7]. However, despite the intensive application of wavelet representations in various image processing tasks, it has been shown that commonly used two-dimensional wavelets, as separable extensions from the one-dimensional domain, have some limitations in capturing geometrical image structures. These limitations come in terms of selective directionality, high anisotropy and sparsity [25]. This fact has motivated the emergence of multiscale geometric transforms, such as curvelets [14] and contourlets [26], in an attempt to address the problem of efficiency in classical multiscale image analysis. Efficiency, here, refers to the ability to provide a sparse representation of significant image information such as the geometry of image edges and the smoothness along image contours. The contourlet transform (CT) not only allows for multiresolution and localization, but also has key features of directionality and anisotropy which enhance its efficiency as a multiscale directional image representation [26]. Therefore, the impact of the contourlet transform on the quality of texture analysis and feature extraction is very promising. Recently, contourlets have been successfully used for texture discrimination and retrieval. Two main approaches have been adopted. The first consists in using energy measures of contourlet subbands as features for texture discrimination [44], while the second is based on statistical modeling of spatial-frequency subbands [35].

Statistical modeling aims at capturing natural characteristics of texture images in a small and compact set of parameters. A variety of these models have been used in applications related to image segmentation [1], multi-temporal SAR image change detection [10], image and video coding [15], texture discrimination and retrieval [2], [18], [19] and image denoising [33]. Randen *et al.* [37] have compared several filtering approaches and have concluded that statistical signatures yield better performance for texture description than energy-based methods. In [35], a study on statistical modeling of CT coefficients in natural images has revealed new properties such as: a) CT coefficients strongly depend on their spatial, multi-scale and directional neighborhood, especially for highly textured images, and b) conditioned on their neighborhood, CT coefficients quite often exhibit "approximate" Gaussian distribution. Based on these properties, a texture retrieval application is developed where neighborhood dependencies in CT subbands are captured using a hidden Markov tree model with mixtures of Gaussians (MoG) [35]. Minimum values of a Kullback-Liebler divergence (KLD) between two image models are used to find similar images. This method has achieved better retrieval rates than using wavelets to search for texture images exhibiting high directionality. Another related approach [27] restricts MoG modeling to intra-band dependencies in luminance images. Directional orientation in each contourlet subband yields Markov dependencies among neighboring coefficients used for model parameter

Manuscript received December 20, 2012; revised March 27, 2013 and July 30, 2013; accepted October 30, 2013. Date of publication January 09, 2014; date of current version March 13, 2014. This work was supported in part by the Natural Sciences and Engineering Research Council of Canada (NSERC) and in part by the Canada Foundation for Innovation (CFI). The associate editor coordinating the review of this manuscript and approving it for publication was Dr. Feng Wu.

The authors are with Computer Science and Engineering, Universite du Quebec en Outaouais, Gatineau, QC J8Y 3T6, Canada (e-mail: mohandsaid.allili@uqo.ca; nadia.baaziz@uqo.ca; marouene.mejrii@uqo.ca).

Color versions of one or more of the figures in this paper are available online at http://ieeexplore.ieee.org.

Digital Object Identifier 10.1109/TMM.2014.2298832

estimation. Further extensions via intra-band dependencies in chrominance components achieve higher retrieval rates at the cost of larger feature vectors.

In [36], the marginal distribution of CT coefficients in each subband has been modeled using a centered generalized Gaussian density (GGD). The GGD parameters (namely scale and shape) are estimated for each CT subband and included as components of the image feature vector. The KLD between GGD models of two images has been used to measure image similarity. In comparison to Laplacian and Gaussian distributions, the GGD has an additional free parameter controlling the shape of the distribution and giving it more flexibility to fit *platykurtic* and *leptokurtic* histogram shapes. In their successive works on texture retrieval, Do *et al.* [23] and Choy *et al.* [18] compared favorably GGD-based wavelet modeling with energy features of wavelet subbands. However, the main assumption in these works is that a single GGD can capture the shape of the wavelet distribution in each subband. When examining several examples of texture images, one might clearly notice that for a wide range of natural texture images, wavelet and CT distribution is heavy-tailed. One can also find a range of images with asymmetrical and/or multi-modal wavelet/CT distribution [6] (see also Fig. 3 in the present paper). In these cases, representation with a single GGD will lack accuracy since it is unimodal. To overcome these limitations, Allili [6] proposed a model based on finite mixtures of GGDs (MoGGs) which has proven to be more efficient than using single GGDs to capture the variety of wavelet coefficients histogram shapes. This property, in turn, allows for more precise texture discrimination and retrieval than using single probability density functions (pdfs), such as the GGD [23] or the generalized Gamma density (GΓD) [19]. Recently, Allili *et al.* [5] have used MoGG modeling for contourlet coefficient representation, which has been proven to be a better alternative than any other distribution (e.g., GGD, GΓD and MoGG) for modeling wavelets in texture discrimination and retrieval applications.

In this paper, we propose to combine contourlets and MoGG modeling for efficient texture image representation. Our main objective is to provide an extensive study for the statistical modeling of contourlets and exploit their properties for efficient texture description and discrimination. In turn, we gain a thorough understanding of the CT properties and their advantages over the wavelet transform to represent fundamental texture visual information, in terms of scale, space and direction. We can briefly summarize our contributions as follows:

- We study MoGG modeling for two implementations of the Contourlet Transform (CT), namely the Standard Contourlet Transform (SCT) [26] and the Redundant Contourlet Transform (RCT) [8], which differ in filtering and down-sampling operations at the multi-scale decomposition stage. The RCT has been proposed by Baaziz [8] for adaptive image watermarking and has shown better results than wavelets. We show in this paper that the RCT lends itself as a better alternative for the SCT in texture discrimination and retrieval applications.
- We validate the performance of the proposed approach using three different applications, namely: (1) texture retrieval, (2) fabric texture defect detection and (3) infrared (IR) face recognition. Texture directionality is a very important aspect for these applications. We show that RCT modeling using MoGGs provides very precise texture signatures than using wavelets and the SCT. Experimental results on standard datasets show that the proposed approach outperforms recent state-of-the-art methods in the aforementioned applications while maintaining comparable computational time.

A short version of this research has been published in [5]. In the present paper, we provide a broader theoretical description of the SCT and RCT, as well as their MoGG modeling. Experimental results validating our approach comprise a more thorough investigation on texture discrimination and retrieval, and two new applications: (1) fabric texture defect detection and (2) infrared (IR) face recognition.

The remainder of this paper is organized as follows: Section II describes relevant properties of the SCT and RCT. Section III gives details about MoGG model learning and similarity measurement between images. Section IV shows results obtained for our three applications. Section V analyzes the computational efficiency of the proposed approach. We end the paper with a conclusion and some future work perspectives.

II. The Contourlet Transform

The contourlet transform (CT) has been developed by Do and Vetterli [25] as an alternative to separable wavelets [21] which are limited in their ability to capture directional information in natural images. The CT is designed explicitly as a true 2D transform that provides multiscale image representation with a high level of directional selectivity and anisotropy. It has been shown that contourlets are well adapted for representing image edges; the CT yields sparse representation and better reconstruction of smooth contours in natural images [26]. Finally, the CT is computationally efficient as it requires $O(N)$ operations for an N-pixel image. The CT's numerous attractive attributes motivate its use in extracting significant image features for texture analysis and retrieval. We now briefly present the standard (SCT) and redundant (RCT) contourlet transforms used in this work.

A. The Standard Contourlet Transform (SCT)

The standard contourlet transform (SCT) [26] is constructed by combining two distinct and successive decomposition stages: a multiscale decomposition followed by a directional decomposition. The multiscale decomposition uses a Laplacian pyramid scheme to transform the image into one coarse version plus a set of Laplacian sub-images (LP). The directional decomposition iteratively applies two-dimensional filtering and critical down-sampling to images. Each LP subband is split into different and flexible number of frequency wedge-shaped subbands allowing to capture geometric structures and directional information in images. In addition to offering perfect reconstruction and high computational efficiency, the SCT is almost critically sampled with a redundancy factor up to 4:3 due to the Laplacian pyramid [13]. When compared to the DWT, the SCT yields some improvements and new potentials in texture analysis applications with its improved directional selectivity [35].

B. The Redundant Contourlet Transform (RCT)

Multiscale image processing applications, where data redundancy is not an issue, can benefit from augmented redundancy using over-sampled image decompositions instead of critically-decimated ones. Thus, it is possible to achieve more accuracy in capturing image features through scales and orientations. This fact has motivated the development of the redundant contourlet transform (RCT) as reported by Baaziz in [8]. The RCT is a variant of the CT, which shares the same decomposition scheme as a double filter bank having multiscale and directional stages. The RCT not only has the main important characteristics of the CT, such as multiresolution, localization, directionality and anisotropy, but also incorporates more redundancy in the multiscale Laplacian pyramid. Redundancy is achieved by eliminating all down-sampling and up-sampling operations from the Laplacian stage, thus reducing aliasing problems and providing equal-size subband images. In addition, the RCT uses new low-pass filters with pseudo-Gaussian properties to generate the scale levels of a decomposed image. As mentioned in [22], Gaussians are known to be the functions used for image representation in the human visual system. Filter impulse responses $g_b(n)$ are finite and symmetric, as given in Eq. (1), where b is a parameter influencing the frequency bandwidth:

$$g_b(n) = \exp\left(-2\frac{n}{b}\right) - \exp(-2)\left(\exp\left(-2\left(\frac{n-b}{b}\right)^2\right) \exp\left(-2\left(\frac{n+b}{b}\right)^2\right)\right). \quad (1)$$

The set of equations below represent the recursive implementation of RLP levels using pseudo-Gaussian filters g_b:

$$I_\ell(m,n) = I_0(m,n) * g_{2^\ell}(m) * g_{2^\ell}(n), \quad (2)$$

$$RLP_\ell(m,n) = I_{\ell-1}(m,n) - I_\ell(m,n), \ell = 1,\ldots,J, \quad (3)$$

where $*$ is the convolution operator, I_0 the original image, I_ℓ and RLP_ℓ are the coarse image approximation and the redundant Laplacian subband at scale level ℓ, respectively. J pseudo-Gaussian filters g_b (with $b = 2^\ell$) are required to generate a redundant Laplacian pyramid (RLP) having $J+1$ equal-size subbands: one coarse image approximation I_a and J band-pass images. Each sub-image has the same size as I_0. Then, applying the contourlet directional filter bank (DFB) with $D = 4$ orientations and 1:4 critical down-sampling on each of the J RLP subbands results into $4J$ equal-size directional subbands ($C_{\ell,d}, \ell = 1,\ldots,J; d = 1,\ldots,D$) in addition to image approximation C_a, which may be down-sampled with factor 1:4. Finally, the RCT achieves a redundancy factor up to $J+1$ due to the redundant Laplacian pyramid stage [8].

Fig. 1 illustrates the multiscale representation and directional partition of the RLP and RCT in the frequency domain. Fig. 2 presents an example of image decomposition that compares between the SCT and RCT. For better visualization, the coefficients of each subband image are put to their absolute values and normalized to the range [0,255]. We can clearly notice that the RCT has a richer description than the SCT in the different subbands. For example, contrarily to the SCT, the size of subband images in lower (coarse) levels is the same as for the first level

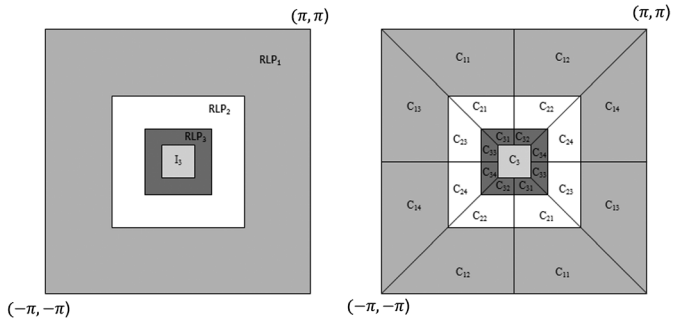

Fig. 1. Frequency partition for: (left) a three-level RLP decomposition, and (right) a three-level RCT decomposition with 4 directions.

in the RCT. As will be shown in the experiments, this property is revealed to be crucial for enhancing the RCT's potential for texture description.

III. RCT-MoGG Modeling and Texture Similarity Measurement

A. MoGG Model Learning

The GGD for a univariate random variable $\mathbf{x} \in \mathbb{R}$ is defined as follows:

$$p(x|\mu,\sigma,\beta) = K(\beta,\sigma)\exp(-A(\beta)|(x-\mu)/\sigma|^\beta), \quad (4)$$

where $K(\beta,\sigma) = \beta\sqrt{\Gamma(3/\beta)/\Gamma(1/\beta)}/(2\sigma\Gamma(1/\beta))$ and $A(\beta) = [\Gamma(3/\beta)/\Gamma(1/\beta)]^{\beta/2}$; $\Gamma(.)$ is the Gamma function. Parameters μ and σ are the GGD location and dispersion parameters. Parameter β controls the *kurtosis* of the pdf and determines whether it is peaked or flat: the larger the value of β, the flatter the pdf; and the smaller the value of β, the more peaked the pdf. This gives the pdf flexibility to fit the shape of heavy-tailed data. For multi-modal data, Allili *et al.* [1] proposed using a mixture of GGDs (MoGG). Given a MoGG with K components and an n-sample dataset $\mathcal{X} = \{x_1, x_2, \ldots, x_n\}$, the likelihood of data is given by:

$$\mathcal{L}(\mathcal{X}|\vec{\theta}) = \prod_{i=1}^{n}\left(\sum_{j=1}^{K}\pi_j p(x_i|\vec{\theta}_j)\right), \quad (5)$$

where $\vec{\theta} = \{\vec{\theta}_j, \pi_j, j = 1,\ldots,K\}$ and $\vec{\theta}_j$ is the complete set of parameters defining each GGD component of the mixture; thus, we have $\vec{\theta}_j = \{\mu_j, \sigma_j, \beta_j\}$, $j = 1,\ldots,K$. We also have these conditions for the mixing parameters $\pi_j, j = 1,\ldots,K$: $0 < \pi_j \leq 1$ and $\sum_{j=1}^{K}\pi_j = 1$. The parameters vector $\vec{\theta}$ and the number of components K are estimated using the *minimum message length principle* (MML) as proposed in [3]. The MML principle is used to select the optimal MoGG model which provides the best tradeoff between data fitting accuracy and model complexity (i.e., number of components K). The message length $MessL$ encoding the contourlet coefficients in a given subband is given by (see [42]):

$$MessL \simeq -\log\left[p(\vec{\theta})\right] + \frac{1}{2}\log\left[|I(\vec{\theta})|\right] + \frac{c}{2}(1+\log\frac{1}{12}) - \log\left[\mathcal{L}(\mathcal{X}|\vec{\theta})\right], \quad (6)$$

where $p(\vec{\theta})$ and $I(\vec{\theta})$ denote, respectively, the prior distribution of parameters $\vec{\theta}$ and the (expected) Fisher information matrix. The constant $c = 4K$ in (6) gives the total number of parameters in the mixture model (refer to [3] and [6] for more details about the choice of priors $p(\vec{\theta})$ and the procedure used to calculate $I(\vec{\theta})$).

The cost function (6) is calculated for different values of K (i.e., $K \in \{K_{\min}, \ldots, K_{\max}\}$), and the optimal number of components K^* is chosen to be the one that minimizes (6). Given a candidate K, we estimate the parameters $\vec{\theta}$ using the expectation-maximization (EM) algorithm, which is based on the interpretation of $\mathcal{X}$ as *incomplete data*. The missing part is a set of n labels $\mathcal{Z} = \{z_1, \ldots, z_n\}$. Each label z_i is a binary vector $z_i = [z_{i,1}, \ldots, z_{i,K}]$, where $z_{i,j} = 1$ if sample x_i is generated by the the jth component of the mixture, and $z_{i,j} = 0$ otherwise. The log-complete likelihood is therefore given by:

$$\log\left[\mathcal{L}(\mathcal{X}, \mathcal{Z}|\vec{\theta})\right] = \sum_{i=1}^{n}\sum_{j=1}^{K} z_{i,j} \log\left[\pi_j p(x_i|\vec{\theta}_j)\right]. \quad (7)$$

The EM algorithm consists of alternating the following two steps for producing a sequence of estimates $\{\vec{\theta}'(t), t = 0, 1, 2, \ldots\}$ until convergence:

- **E-step:** Consists of computing the expectation of the complete log-likelihood:

$$Q(\vec{\theta}, \vec{\theta}'(t)) = E_z\left[\log(\mathcal{L}(\mathcal{X}, \mathcal{Z}|\vec{\theta}(t)))|\vec{\theta}', \mathcal{X}\right], \quad (8)$$

  where $\vec{\theta}'(t)$ is the current estimate of $\vec{\theta}$.
- **M-step:** Consists of updating parameter estimates $\vec{\theta}$ by maximizing function $Q(\vec{\theta}, \vec{\theta}')$ according to $\vec{\theta}$. This is given by the formula:

$$\vec{\theta}'(t+1) = \arg\max_{\vec{\theta}}\left(Q(\vec{\theta}, \vec{\theta}'(t)) + \log p(\vec{\theta})\right). \quad (9)$$

Fig. 3 shows the approximation of the SCT and RCT subbands of the texture image 'Tile 1' in Fig. 2. Notice the shape of subband coefficients histograms, which is sharply peaked, heavy-tailed and asymmetric at the same time. The MoGG model gives a very accurate approximation of these histograms. We can note the difference in the higher subband levels between the SCT and the RCT. In fact, the RCT has more accurate signatures than the SCTs thanks to the redundancy that provides enough data for better histogram approximation.

B. MoGG *Similarity Measurement*

Many past works demonstrated the advantage of using the KLD to calculate discrepancies between statistical distributions in the context of texture discrimination [6], [18], [19], [23], [24]. When distribution of contourlet coefficients can be approximated using univariate and centered GGDs, a closed-form solution for the KLD between two subbands in different images can be formulated [18], [23]. However such a solution in our case is hard to achieve since the subbands are modeled using mixtures with arbitrary numbers of GGDs. To overcome this problem, we resort to approximating the KLD using Monte-Carlo sampling methods, as proposed in the work of Allili [6]. In that work, different approximation methods, namely: *Monte-Carlo sampling* and *variational lower-bounds* have been compared for their accuracy. It has been shown that Monte-Carlo sampling techniques are the most accurate. Briefly, given two MoGG models $p(x|\vec{\theta}) = \sum_{i=1}^{K}\pi_i p(x|\vec{\theta}_i)$ and $p(x|\vec{\varphi}) = \sum_{j=1}^{M}\omega_j p(x|\vec{\varphi}_j)$, the KLD between these models is defined as [20]:

$$\mathrm{KLD}(p(x|\vec{\theta})||p(x|\vec{\varphi})) = \int_x p(x|\vec{\theta})\log\left(\frac{p(x|\vec{\theta})}{p(x|\vec{\varphi})}\right)dx. \quad (10)$$

Sampling methods aim to generate a sufficiently large sample $\mathcal{X} = \{x_1, x_2, \ldots, x_n\}$, drawn independently from the distribution $p(x|\vec{\theta})$, in order to approximate the expectation of the KLD using the Monte-Carlo integration:

$$\mathrm{KLD}_{mc}\left(p(\cdot;|\vec{\theta})||p(\cdot;x|\vec{\varphi})\right) = \frac{1}{n}\sum_{i=1}^{n}\log\left[\frac{p(x_i|\vec{\theta})}{p(x_i|\vec{\varphi})}\right] + \frac{p(x_i|\vec{\varphi})}{p(x_i|\vec{\theta})} - 1. \quad (11)$$

This approximation converges to the true $\mathrm{KLD}(p(x|\vec{\theta})||p(x|\vec{\varphi}))$ when $n \to \infty$. The term $p(x_i|\vec{\varphi})/p(x_i|\vec{\theta}) - 1$ in (11) is added to the Monte-Carlo integration to ensure that $\mathrm{KLD}_{mc} \geq 0$ [34]. In [4], we have tested both Metropolis-Hastings and Accept-Reject sampling methods [38] and have concluded that the latter is better suited to approximate the true KLD between two MoGG models.

Finally, given an J-level RCT, the pyramidal decomposition of each image will result into $4J$ high-pass subbands: $C_{\ell,1}, C_{\ell,2}$, $C_{\ell,3}$ and $C_{\ell,4}$, $\ell \in \{1, \ldots, J\}$, and one low-pass subband C_a. Therefore, similarity between a query image I_Q and a target image I_T can be calculated by summing up the KLD approximations between all corresponding subbands in I_Q and I_T, as follows:

$$\mathcal{S}(I_Q, I_T) = \sum_{\ell=1}^{J}\sum_{d=1}^{4}\left(\mathrm{KLD}_{mc}(f_Q^{(\ell,d)}\|f_T^{(\ell,d)})\right) + \mathrm{KLD}_{mc}\left(f_Q^{(a)}\|f_T^{(a)}\right), \quad (12)$$

where $f_Q^{(\ell,d)}$ and $f_T^{(\ell,d)}$ represent the MoGG models calculated in the two images I_Q and I_T for the subband of the ℓ-th level and the d-th direction, respectively. Likewise, $f_Q^{(a)}$ and $f_T^{(a)}$ designate the MoGG models calculated for the approximations of images I_Q and I_T, respectively.

IV. Experimental Results

To measure the performance of the proposed approach, we conducted experiments grouped into three applications. In the first application, we used our contourlet modeling to address the texture retrieval problem. In the second application, we used our approach to detect fabric texture defects. In the third application, our approach was used for infrared (IR) face recognition. In the following sub-sections, each application is developed separately.

A. Texture Retrieval

In this application, we conducted experiments using images from the Brodatz [12] and VisTex [32] texture datasets. In each dataset, we choose 47 images with different texture structures

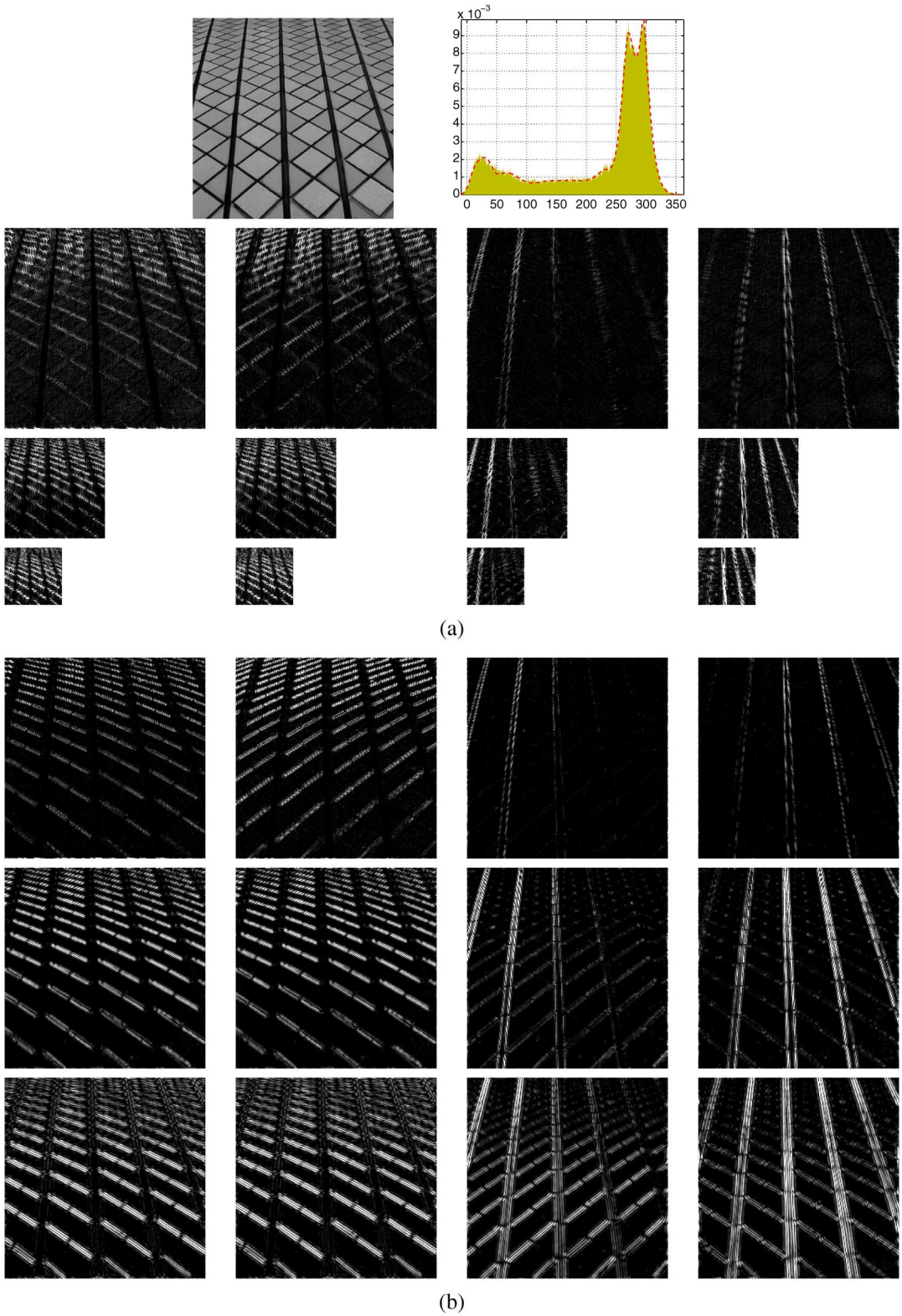

Fig. 2. Example comparing the SCT (a) with the RCT (b). The first row represents the texture image (ref. Tile 1 in the VisTex database [32]) and the histogram of the image approximation fitted using a MoGG model. For each transform, from left to right, we show subbands $C_{\ell,1}$, $C_{\ell,2}$, $C_{\ell,3}$ and $C_{\ell,4}$, $\ell \in \{1,2,3\}$, respectively. From top to bottom, we show subband levels $C_{1,d}$, $C_{2,d}$ and $C_{3,d}$, $d \in \{1,2,3,4\}$, respectively.

and orientations. Each image has 512×512 pixel size and is divided into sixteen 256×256 sub-images, thus creating a database of $\mathcal{M} = 752$ sub-images and 47 texture classes in each dataset. To eliminate the effect of range variation in the luminance of the sub-images, and thus reduce bias in the retrieval phase, we normalized the luminance of each sub-image as follows. Let μ_M and σ_M be the medians of the means and the standard deviations of the 16 sub-images stemming from the same image. Each sub-image $I^{(i)}$ of the 16 is normalized using the following formula: $I^{(i)} = \frac{\sigma_M}{\sigma_i}(I^{(i)} - \mu_i) + \mu_M$, where μ_i

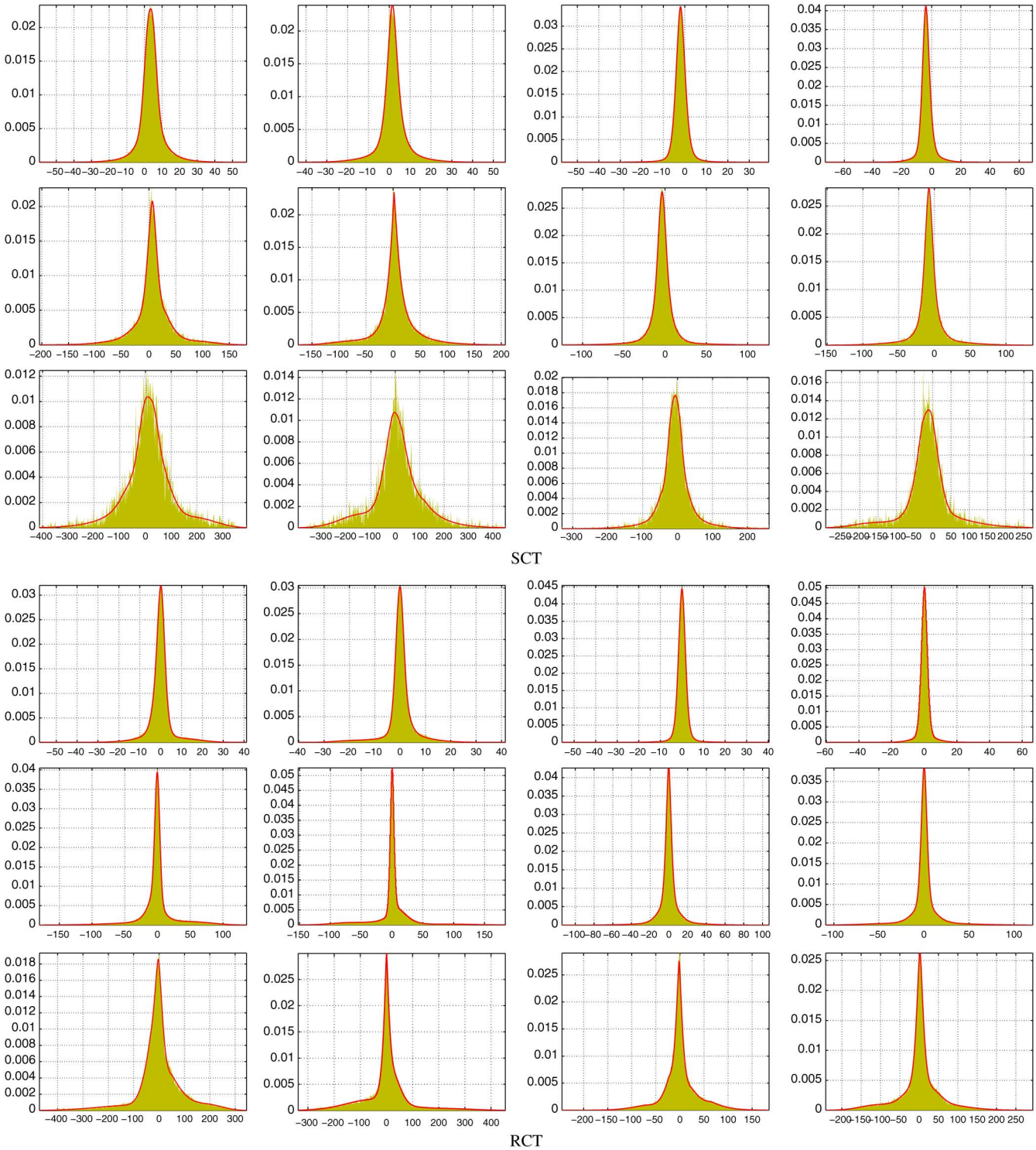

Fig. 3. Example comparing SCT with RCT coefficient representation of the texture image in Fig. 2, using MoGG modeling (red curve). For each transform, from top to bottom we show levels 1, 2 and 3, respectively. From left to right, we show subbands $C_{\ell,1}$, $C_{\ell,2}$, $C_{\ell,3}$ and $C_{\ell,4}$ for each level ℓ, respectively.

and σ_i are the mean and standard deviation of $I^{(i)}$, respectively. To show the advantage of using RCT instead of SCT, we measured for each transform the intra-class variation of the KLD corresponding to (high-pass) lower subband levels (i.e., $\ell = 2, 3$) where the transforms differ in their sampling. Table I shows the obtained results for all images in the VisTex and Brodatz databases. Clearly, signatures obtained using the RCT have lower variance than those obtained using the SCT, thanks to sampling redundancy which gave more stable MoGG models between images sharing the same class label. As will be shown in the rest of the experiments, this property plays a key role in enhancing texture discrimination and retrieval performance.

In what follows, we measure retrieval performance in terms of *the retrieval rate* (%), which refers to *the fraction of the number of relevant images found among the top-N retrieved images*. More formally, the retrieval rate for each query is given

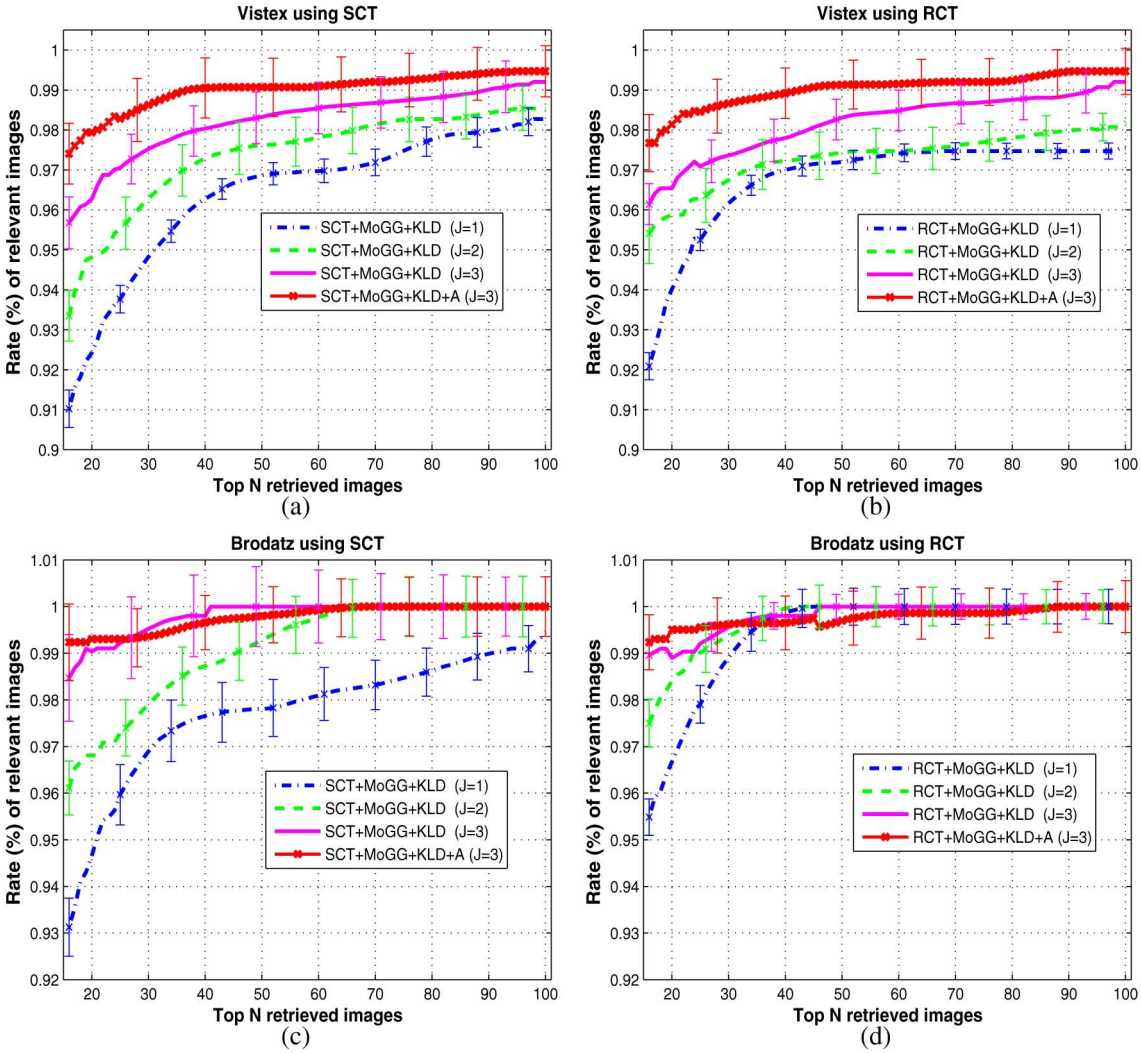

Fig. 4. Average retrieval rates of 235 queries as a function of the number of top matches considered, using the standard (SCT) and redundant (RCT) contourlet transforms: (a,b) and (c,d) show results for the Vistex and Brodatz databases, respectively.

TABLE I
AVERAGE INTRA-CLASS VARIANCE OF THE KLD CALCULATED FOR LOWER HIGH-PASS SUBBANDS OF THE SCT AND RCT, RESPECTIVELY

Level	SCT	RCT	% of variance reduction
$\ell = 2$	6.27×10^{-1}	5.07×10^{-1}	19.20%
$\ell = 3$	8.86×10^{-1}	5.40×10^{-1}	39.01 %

as: $RR = RI * 100/R$, where RI is the number of relevant images among top N retrieved images, and R is the total number of relevant images which is always 16 in our case. In each dataset, the final retrieval rate is calculated by averaging retrieval rates corresponding to $235 = 5 \times 47$ randomly-selected queries (5 random queries for each image category). In a first test, we compared the standard (SCT) and redundant (RCT) contourlet transforms for the two datasets. Fig. 4 shows this comparison using different combinations of decomposition levels; we refer to these tests as $(\mathrm{SCT}/\mathrm{RCT}) + \mathrm{MoGG} + \mathrm{KLD}$ $(J = 1, 2, 3)$, respectively. We also conducted a test combining high- and low-pass subbands for texture retrieval, referred to as $(\mathrm{SCT}/\mathrm{RCT}) + \mathrm{MoGG} + \mathrm{KLD} + \mathrm{A}$ $(J = 3)$. We included for each test the standard deviation of retrieval rates for different numbers of top-retrieved images. We can note that for both the Vistex and Brodatz datasets, increasing the number of levels of decomposition always increases the texture retrieval rate. However, the RCT yields better search accuracy than the SCT. Moreover, the SCT has a slightly larger standard deviation of retrieval rates than the RCT, which goes in line with our results in Table I. Finally, Table II shows retrieval rates for top 16 retrieved images by considering different levels of decomposition and combining low- and high-pass subbands, respectively. The RCT clearly yields better results than the SCT for all combined levels. In addition, including the approximation subband improves the retrieval performance for both the SCT and the RCT.

In another experiment, we compared our method with three recent works in texture retrieval, namely: (1) $\mathrm{DWT} + \mathrm{GGD} + \mathrm{KLD}$: Wavelet-based texture retrieval using single GGD signature [23], (2) $\mathrm{DWT} + \mathrm{G\Gamma D} + \mathrm{KLD}$: Wavelet-based texture retrieval using generalized Gamma density GΓD signature [19] and (3) $\mathrm{DWT} + \mathrm{MoGG} + \mathrm{KLD} + \mathrm{A}$: Wavelet-based texture retrieval using MoGG signature [6]. In addition, we implemented the $\mathrm{RCT} + \mathrm{GGD} + \mathrm{KLD}$ and $\mathrm{RCT} + \mathrm{G\Gamma D} + \mathrm{KLD}$ methods, which use the GGD and the GΓD to model the RCT coefficient distribution, respectively. Note that in the first two methods as

TABLE II
AVERAGE RETRIEVAL RATE (%) IN THE TOP 16 IMAGES VERSUS THE NUMBER OF DECOMPOSITION LEVELS USING OUR APPROACH WITH THE SCT AND RCT, RESPECTIVELY

Value of J	DWT+MoGG+KLD		SCT+MoGG+KLD		RCT+MoGG+KLD	
	Vistex	Brodatz	Vistex	Brodatz	Vistex	Brodatz
$J = 1$	90.41%	92.90%	91.02%	93.13%	92.09%	95.40%
$J = 2$	92.65%	95.61%	93.25%	96.11%	95.41%	97.45%
$J = 3$	94.15%	97.35%	95.31%	98.40%	96.14%	98.86%
$J = 3$ + approximation (A)	96.86%	98.61%	96.91%	99.05%	97.41%	99.24%

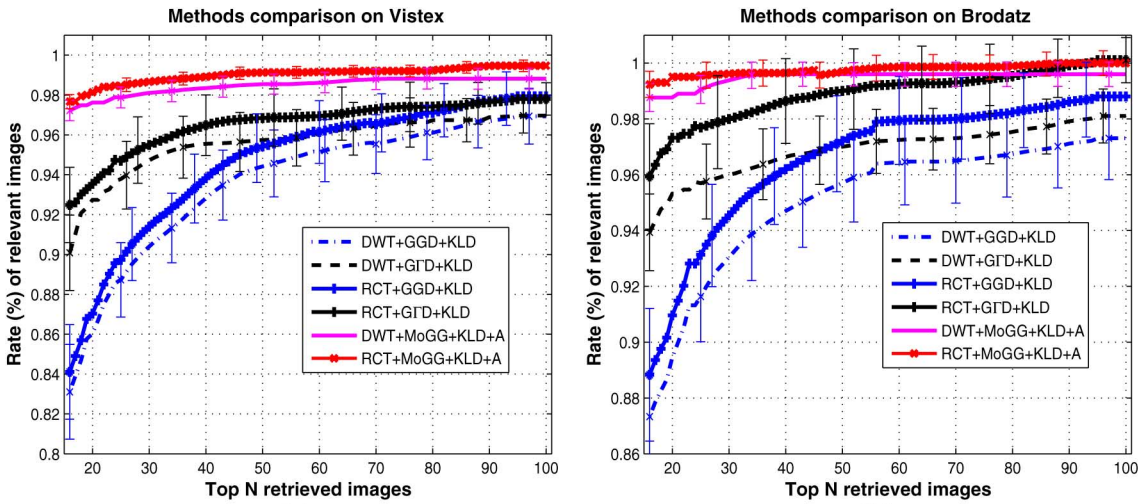

(a) (b)

Fig. 5. Average retrieval rates of 235 queries as a function of the number of top matches considered for the (a) VisTex and (b) Brodatz databases. For each database, we show obtained retrieval rates using DWT + GGD + KLD, RCT + GGD + KLD, DWT + GΓD + KLD, RCT + GΓD + KLD, DWT + MoGG + KLD + A and RCT + MoGG + KLD + A methods, respectively.

well as in RCT + GGD + KLD and RCT + GΓD + KLD, only high-pass subbands were used since low-pass coefficients cannot be approximated using the GGD or the GΓD. In the third method, however, the low- and high-pass DWT subbands were combined in the similarity measurement. We also combined three levels of decomposition for each method.

Fig. 5 shows a comparison of our approach (RCT + MoGG + KLD + A) with the other ones. Our results are in line with [19] in that using GΓD modeling yields better results than using GGD modeling of Vistex and Brodatz database images, and for both DWT and RCT, respectively. We can also note that our approach improves the work in [6] based on DWT, which proves the advantage of modeling texture using the RCT over wavelets. For the top 16 images alone, in the Vistex database (resp. Brodatz database), our approach improves DWT + MoGG + KLD + A by $\approx$ 2% (resp. $\approx$ 2.5%), DWT + GΓD + KLD by $\approx$ 7.6% (resp. $\approx$ 3.32%), RCT + GΓD + KLD by $\approx$ 5.3% (resp. $\approx$ 5.2%), DWT + GGD + KLD by $\approx$ 14.6% (resp. $\approx$ 13.89%) and RCT + GGD + KLD by $\approx$ 14.6% (resp. $\approx$ 10.54%). Finally, Fig. 6 shows textures that are better retrieved using the RCT rather than wavelets (by at least 5%). We can notice that these images exhibit some diversity in the directional content which is better represented using the RCT than using the SCT or DWT.

B. Texture Fabric Defect Detection

Textile industry is a field where automated inspection using image processing techniques is highly needed in order to control the quality of fabrics after manufacturing [17], [30]. Indeed, human inspection is very costly, and tedious and the reliability of visual inspection decreases quickly with fatigue and inattentiveness. The topic of automatic defect detection has been investigated in several works in the last two decades where numerous approaches have been proposed. We emphasize, however, that the goal of our work is to demonstrate the application of the proposed RCT + MoGG modeling for texture defect detection, and compare our approach to similar modeling techniques. Thus, giving an exhaustive review of automated texture defect detection is beyond the scope of this paper.

For our tests, we used the reference TILDA database [41]. It contains a total of 8 representative types of textile, and each type has one of 7 types of defects, or be free of any defect. For each of these classes, there are 50 gray-scale images of 768×512 pixels, making the size of the database $m = 8 \times 8 \times 50 = 3200$ images. Fig. 7(a) and 7(b) show some images of the TILDA database that are defect-free and containing defects, respectively. For a given textile type, our algorithm subdivides first each tested image into blocks, where each block undergoes a multiscale decomposition using DWT + MoGG, SCT + MoGG and RCT + MoGG modeling, respectively. Then, each block B_i is compared to a reference defect-free block B_r. The block B_i is declared as containing defect(s) if $\mathrm{KLD}(B_r, B_i) > \delta_d$, where δ_d is a threshold that is determined experimentally. We note that values of δ_d that are too large will increase the missing of defective blocks, whereas values that are too small will increase the false detection rate. To determine the optimal threshold, we resorted to a learning-based approach:

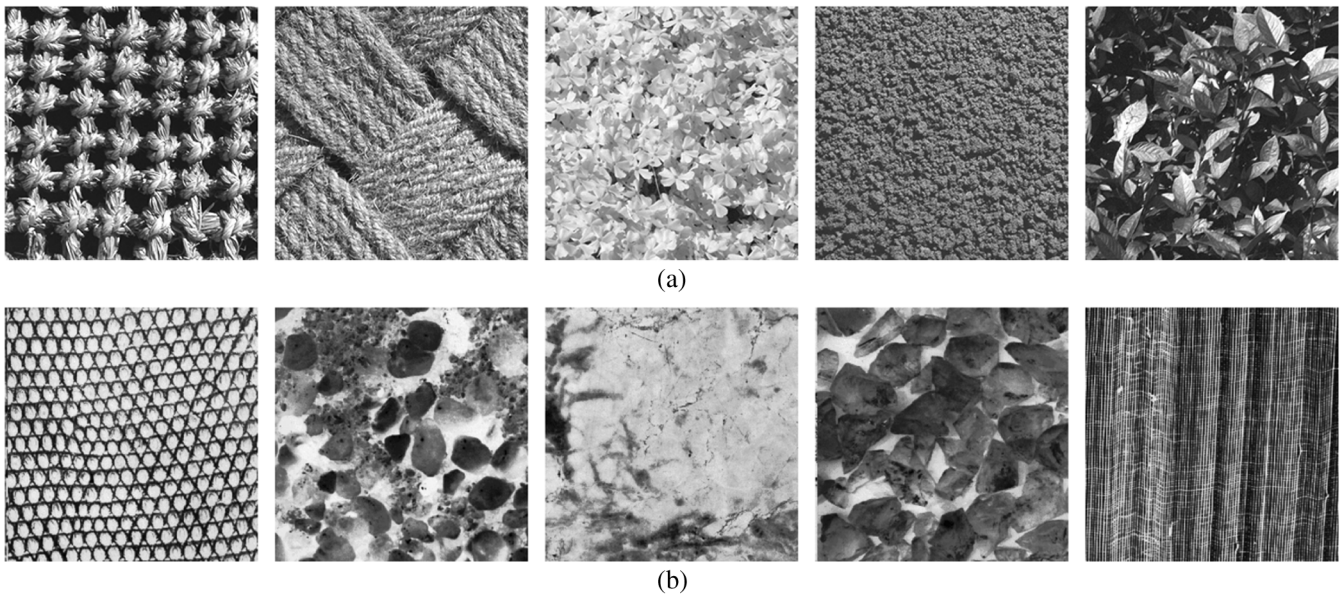

Fig. 6. A sample of textures better retrieved using the RCT than using the DWT (improvement by at least 5%) in: (a) VisTex database and (b) Brodatz database, respectively.

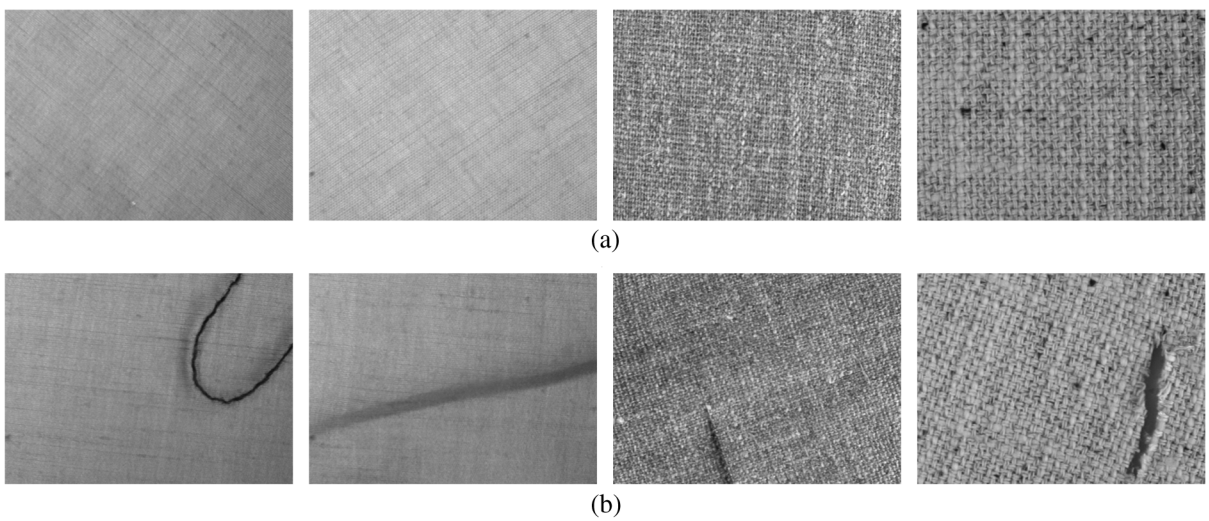

Fig. 7. Examples of images in the TILDA database: (a) without defects, (b) with defects.

Starting from a set of defect-free and defective images of each textile type, a reference defect-free block B_r is extracted (the first block of the first defect-free image might be taken). Let $\mathcal{B} = \{B_1, \ldots, B_n\}$ and $\tilde{\mathcal{B}} = \{\tilde{B}_1, \ldots, \tilde{B}_m\}$ be two sets of defect-free and defective blocks, respectively, for which we calculated the KLD with B_r. The obtained sets of distances are $\mathcal{D} = \{d_1, \ldots, d_n\}$ and $\tilde{\mathcal{D}} = \{\tilde{d}_1, \ldots, \tilde{d}_m\}$, for $\mathcal{B}$ and $\tilde{\mathcal{B}}$, respectively. The threshold δ_d is then calculated using the improved Otsu's method proposed in [11], which gives the best separation between two classes in the presence of multi-modal and heavy-tailed data. In this method, each class is modeled using a MoGG, and the optimal threshold calculation is based on likelihood maximization.

Fig. 8 shows some examples of defect detection using 128×128 and 64×64 block sizes, respectively. The values of m and n are set to 200. We also show defect detection results obtained from applying the independent component analysis method (ICA) described in [39]. During the learning phase, the method uses the *fast-ICA algorithm* [28] to estimate an ICA basis of dimension 16 on a set of defect-free image blocks. This basis is used to calculate a mean feature vector S_{mean} as a representative of any defect-free image block. In the application phase, each block of an incoming test image is decomposed on the ICA basis to extract a feature vector. An image block is classified as defective or non defective according to the Euclidian distance between its feature vector and S_{mean}. Four main observations can be made on the results (see Fig. 8). First, using multiscale decomposition and MoGG modeling outperforms ICA approach in the ability to detect various textile defects as shown in the figure. Second, using contourlets usually allows for more accurate defect detections than using wavelets. This performance is justified

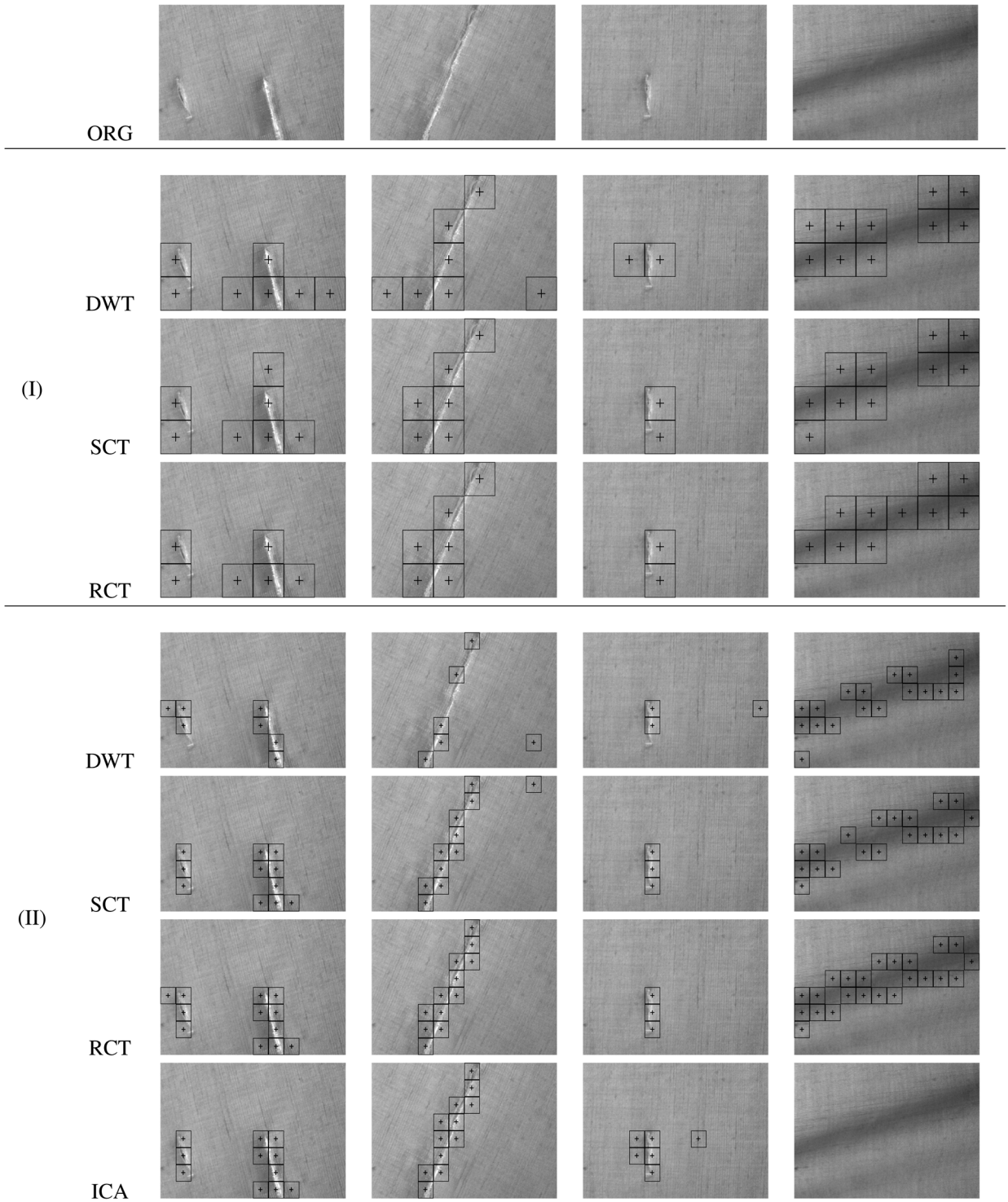

Fig. 8. Examples of defect detection results using (I) 128×128 block size and (II) 64×64 block size. The first row represents original images. For both (I) and (II), the first, second and third rows represent defect detection results obtained using $\mathrm{DWT} + \mathrm{MoGG} + \mathrm{KLD}$, $\mathrm{SCT} + \mathrm{MoGG} + \mathrm{KLD}$ and $\mathrm{RCT} + \mathrm{MoGG} + \mathrm{KLD}$ methods, respectively. The last row in (II) represents results obtained using ICA-based method [39].

by the ability of contourlets to encode directional information more efficiently than using wavelets. Third, the RCT slightly outperforms the SCT thanks to added redundancy to the subbands and pseudo-Gaussian filters in the RCT, which allow for better texture discrimination. Fourth, using a block size of 64×64 pixels locates defects more precisely than using a 128×128 block size. This performance is justified by the fact that smaller blocks allow for more detailed delineation of defects and, therefore, for more accurate detections.

Finally, to compare the performance of our method quantitatively, we used the *error rate* measure which gives *the rate of incorrectly classified blocks among all image blocks*. More formally, suppose that an image contains L blocks and that a defect detection algorithm assigns a label $\ell_i = 1$ if a block B_i

TABLE III
AVERAGE VALUES OF ε OBTAINED FOR $\mathrm{DWT} + \mathrm{MoGG} + \mathrm{KLD}$, $\mathrm{SCT} + \mathrm{MoGG} + \mathrm{KLD}$, $\mathrm{RCT} + \mathrm{MoGG} + \mathrm{KLD}$ AND ICA [39]

Method	DWT+MoGG+KLD		SCT+MoGG+KLD		RCT+MoGG+KLD		ICA
Block size	128×128	64×64	128×128	64×64	128×128	64×64	64×64
$J = 1$	09.17%	06.83%	06.53%	02.67%	06.11%	02.64%	03.61%
$J = 1$ + approximation (A)	08.61%	05.73%	05.83%	02.60%	05.97%	02.60%	

Fig. 9. Examples of IR images in the Terravic database.

is detected as defective and 0 otherwise. We also suppose that $\tilde{\ell}_i$ is the ground truth label of block B_i. The *error rate* can be calculated with this formula:

$$\varepsilon = \sum_{i=1}^{L} |\ell_i - \tilde{\ell}_i|/L. \tag{13}$$

Table III gives average values of ε calculated for a set of 30 images from the TILDA database, using 128×128 and 64×64 block sizes, respectively. In the MoGG modeling approach, the best defect detection performance was obtained using the first level of multiscale decomposition ($J = 1$) combined with the approximation (A); we show the corresponding ε values on the table. We can also note that contourlets yield better results than wavelets and ICA methods, and that the RCT generally outperforms the SCT.

C. Infrared Face Recognition

Face recognition is a fast growing research area in image processing due to increasing demands for security in commercial and law enforcement applications [45]. While face recognition in the visible spectrum has been investigated extensively over the last two decades [31], thermal IR face recognition has received relatively little attention. The IR spectrum can be used to identify faces when there is little or no control over lighting conditions [16]. This advantage is supported by the fact that thermal emissions from the skin are an intrinsic property, independent of illumination. Thus, face images captured using IR sensors are expected to be nearly invariant to changes in illumination conditions. Wilder *et al.* [43] demonstrated that both visible and IR methods perform similarly across several algorithms. A comprehensive review of recent face recognition techniques using the IR spectrum can be found in [29] and [31].

In this paper, we propose to use our $\mathrm{RCT} + \mathrm{MoGG}$ modeling for face recognition in the IR spectrum. We use the popular Terravic IR face database [40] which contains 24 508 images. The database contains 20 classes, each of which contains images of the same person's face viewed in full frontal, left and right profile, respectively. A person may also wear glasses or not during acquisition. Fig. 9 shows some examples of faces from the database. In a first experiment, we compared our results with those obtained in the work [9] which uses *eigenface decomposition* on either Haar wavelets transform (HWT) or *local binary pattern* (LBP) to extract features for face recognition. In that work, the authors used different combinations of visible and IR features on a set of 578 images from the Terravic dataset. Half of this set was taken to calculate the eigenfaces and the other half for testing face recognition. A query face is recognized when the closest images in the database are from the same person. We adopted the same experiment setting for our approach by using $(\mathrm{DWT}/\mathrm{SCT}/\mathrm{RCT}) + \mathrm{MoGG}$ signatures instead of eigenfaces. Moreover, we used the KLD approximation (12) to calculate similarity between faces. Table IV shows results of the obtained face recognition rates. We can clearly notice that using $(\mathrm{DWT}/\mathrm{SCT}/\mathrm{RCT}) + \mathrm{MoGG}$ signatures outperform the standard eigenface decomposition methods using HWT and LBP features, respectively. Furthermore, RCT led to the highest recognition rate compared to the SCT and DWT. This experiment demonstrates the great potential of our approach for IR face recognition.

TABLE IV
COMPARISON OF AVERAGE FACE RECOGNITION RATES IN THE TERRAVIC DATABASE USING EIGENFACE DECOMPOSITION VS. $(\mathrm{DWT}/\mathrm{SCT}/\mathrm{RCT}) + \mathrm{MoGG}$ SIGNATURES

Method	Eigenface decomposition		MoGG+KLD		
	HWT	LBP	DWT	SCT	RCT
Recognition rate	95.09 %	94.11%	98.56%	99.38%	99.88%

In a second experiment, we compared DWT, SCT and RCT for IR face retrieval application. We performed 5 randomly-selected queries in the dataset for each face class, making a total of 100 queries. Fig. 10 shows graphs obtained for the average retrieval rate as a function of the number of top retrieved faces. Fig. 10(a) shows the performance obtained for different decomposition levels in the RCT. The best performance is clearly obtained using $J = 2$, which reveals that for IR images, structural information is contained mainly in the first two levels. Surprisingly, the combination of high- and low-pass coefficients leads to the worst result of all the compared methods (DWT, SCT and RCT). This can mainly be justified by the fact that, contrarily to the first and second applications, where the image luminance is a main factor for discrimination, histograms of IR face images are very similar overall different faces. Thus, they do not add much discrimination between different faces. This experiment demonstrates, among other things, the limitations of using the approximation for texture discrimination. Finally, Fig. 10(b) compares

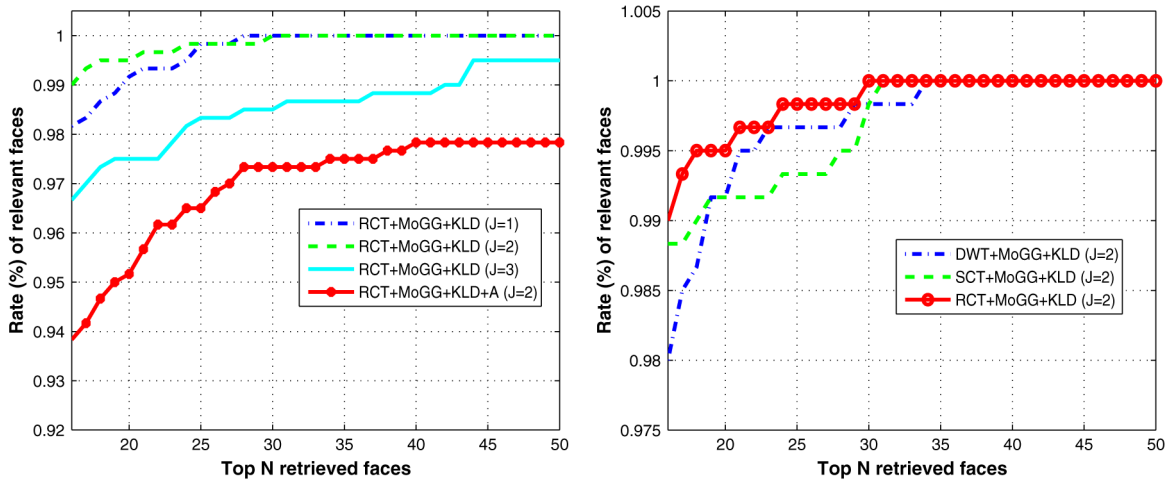

Fig. 10. Average retrieval rate of 40 queries as a function of the number of top retrieved faces: (a) results obtained for the RCT using different levels of decomposition, (b) results obtained using DWT + MoGG + KLD, SCT + MoGG + KLD and RCT + MoGG + KLD methods, respectively.

face recognition performance between DWT+MoGG+KLD, SCT+MoGG+KLD and RCT+MoGG+KLD methods. We can note that contourlets generally outperform wavelets by an average of $\approx 1\%$. The RCT slightly outperforms the SCT for the same values of top retrieved faces by an average of $\approx 0.5\%$.

V. Computational Efficiency

The EM algorithm for the estimation of K-components MoGG model using N CT coefficients requires a computational time of order $O(KN)$ [6]. The computational time of calculating image similarity using Eq. (12) is $O(JKn)$, where J is the number of RCT decomposition levels. It follows that the complexity of performing a query in a database of size $\mathcal{M}$ is $O(JK\mathcal{M}n)$, where n is the number of generated samples. The same computational time is required to conduct an IR face recognition. Given an image of L blocks, defect detection in the image has computational complexity $O(J\bar{K}nL)$, where $\bar{K}$ is the number of MoGG components of the reference block. Currently, all our experiments are performed in the Matlab environment running on a workstation with a 3.5 GHz Intel processor. In the texture retrieval application, the average CPU time for a query is about 8 seconds, whereas the equivalent amount of time is 1.0 seconds using the closed-form KLD proposed in [23]. For the defect detection application, an image of 512×512 pixels is analyzed in 10 seconds. Finally, in the IR face recognition application, a face query is processed in about 5 seconds.

VI. Conclusions

We have proposed a new framework using MoGG statistical modeling of contourlets. In this framework, we have combined low- and high-pass RCT coefficients for texture description and discrimination. We have successfully applied our approach to texture discrimination and retrieval, fabric texture defect detection and IR face recognition. Our approach has yielded better results than recent state-of-the-art methods using the DWT and SCT for texture representation. Future works will focus on extending our approach to color images and video retrieval, as well as reducing the computational time of distance calculation between MoGG models.

References

[1] M. S. Allili, D. Ziou, N. Bouguila, and S. Boutemedjet, "Image and video segmentation by combining unsupervised generalized Gaussian mixture modelling and feature selection," *IEEE Trans. Circuits and Syst. Video Technol.*, vol. 20, no. 10, pp. 1373–1377, 2010.

[2] M. S. Allili, "Wavelet-based texture retrieval using a mixture of generalized Gaussian distributions," in *Proc. IEEE Int. Conf. Pattern Recognition*, 2010, pp. 3143–3146.

[3] M. S. Allili, N. Bouguila, and D. Ziou, "Finite general Gaussian mixture modelling and application to image and video foreground segmentation," *J. Electron. Imag.*, 2008, 17:013005.

[4] M. S. Allili, Similarity measurements between finite mixtures of generalized Gaussian distributions, Tech. rep., 2011.

[5] M. S. Allili and N. Baaziz, "Contourlet-based texture retrieval using a mixture of generalized Gaussian distributions," in *Proc. Int. Conf. Computer Analysis of Images and Patterns*, 2011, no. 2, pp. 446–454.

[6] M. S. Allili, "Wavelet modeling using finite mixtures of generalized Gaussian distributions: Application to texture discrimination and retrieval," *IEEE Trans. Image Process.*, vol. 21, no. 4, pp. 1452–1464, 2012.

[7] A. N. Akansu and P. R. Haddad, Multiresolution Sign. Decomp.: Transforms, Subbands, and Wavelets, A-P, 2000.

[8] N. Baaziz, "Adaptive watermarking schemes based on a redundant contourlet transform," in *Proc. IEEE Int. Conf. on Image Processing*, 2005, pp. I-221–I-224.

[9] D. Battacharjee, A. Seal, S. Ganguly, M. Nasipuri, and K. Basu, "A comparative study of human thermal face recognition based on Haar wavelet transform and local binary pattern," *Computat. Intell. Neurosci.*, pp. 1–12, 2012, Article ID-2610889.

[10] Y. Bazi, L. Bruzzone, and F. Melgani, "An unsupervised approach based on the generalized Gaussian model to automatic change detection in multitemporal SAR images," *IEEE Trans. Geosci. Remote Sens.*, vol. 43, no. 4, pp. 874–887, 2005.

[11] A. Boulmerka and M. S. Allili, "Thresholding-based segmentation revisited using mixtures of generalized Gaussian distributions," in *Proc. IEEE Int. Conf. Pattern Recognition*, , 2012, pp. 2894–2897.

[12] "Brodatz texture database," [Online]. Available: http://www.ux.uis.no/tranden/brodatz.html

[13] P. J. Burt and E. H. Adelson, "The Laplacian pyramid as a compact image code," *IEEE Trans. Commun.*, vol. 31, no. 4, pp. 532–540, 1983.

[14] E. J. Candes and D. L. Donoho, "New tight frames of curvelets and optimal representations of objects with piecewise-C2 singularities," *Commun. Pure Appl. Math.*, vol. 57, pp. 219–266, 2002.

[15] S. G. Chang, Y. Bin, and M. Vetterli, "Adaptive wavelet thresholding for image denoising and compression," *IEEE Trans. Image Process.*, vol. 9, no. 9, pp. 1532–1546, 2000.

[16] X. Chen *et al.*, "IR and visible light face recognition," *Comput. Vision Image Understand.*, vol. 99, no. 3, pp. 332–358, 2005.
[17] C. S. Cho, B. M. Chung, and M. J. Park, "Development of real-time vision-based fabric inspection system," *IEEE Trans. Ind. Electron.*, vol. 52, no. 4, pp. 1073–1079, 2005.
[18] S.-K. Choy and C.-S. Tong, "Supervised texture classification using characteristic generalized Gaussian density," *J. Math. Imag. Vision*, vol. 29, no. 1, pp. 37–47, 2007.
[19] S.-K. Choy and C.-S. Tong, "Statistical wavelet subband characterization based on generalized gamma density and its application in texture retrieval," *IEEE Trans. Image Process.*, vol. 19, no. 2, pp. 281–289, 2010.
[20] T. M. Cover and J. A. Thomas, *Elements of Information Theory*. New York, NY, USA: Wiley, 2006.
[21] I. Daubechies, "Orthonormal bases of compactly supported wavelets," *Commun. Pure Appl. Math*, vol. 41, pp. 909–996, 1988.
[22] J. G. Daugman, "Complete discrete 2-0 Gabor transforms by neural networks for image analysis and compression," *IEEE Trans. Acoust., Speech, Signal Process.*, vol. 36, no. 7, pp. 1169–1179, 1988.
[23] M. N. Do and M. Vetterli, "Wavelet-based texture retrieval using generalized Gaussian density and KLD," *IEEE Trans. Image Process.*, vol. 11, no. 2, pp. 146–158, 2002.
[24] M. N. Do and M. Vetterli, "Rotation invariant texture characterization and retrieval using steerable wavelet-domain hidden Markov models," *IEEE Trans. Multimedia*, vol. 4, no. 4, pp. 517–527, 2002.
[25] M. N. Do and M. Vetterli, *Contourlets, Beyond Wavelets*, G. V. Wellard, Ed. New York, NY, USA: Academic, 2003.
[26] M. N. Do and M. Vetterli, "The contourlet transform: An efficient directional multiresolution image representation," *IEEE Trans. Image Process.*, vol. 14, no. 12, pp. 2091–2106, 2005.
[27] Z. He and M. Bystrom, "Color texture retrieval through contourlet-based hidden Markov model," in *Proc. IEEE Int. Conf. Image Processing*, 2005, pp. 513–516.
[28] A. Hyvarinen, "Fast and robust fixed-point algorithms for independent component analysis," *IEEE Trans. Neural Netw.*, vol. 10, no. 3, pp. 626–634, 1999.
[29] G. Kong, J. Heo, B. R. Abidi, J. Paik, and M. Abidi, "Recent advances in visual and infrared face recognition: A review," *Comput. Vision Image Understand.*, vol. 97, no. 1, pp. 103–135, 2005.
[30] A. Kumar, "Computer-vision-based fabric defect detection: A survey," *IEEE Trans. Ind. Electron.*, vol. 55, no. 1, pp. 348–362, 2008.
[31] S. Z. Li and A. K. Jain, *Handbook of Face Recognition*, 2nd ed. New York, NY, USA: Springer, 2011.
[32] "Vision texture database," [Online]. Available: http://vismod.media.mit.edu/
[33] P. Moulin and J. Liu, "Analysis of multiresolution image denoising schemes using generalized Gaussian and complexity schemes," *IEEE Trans. Inf. Theory*, vol. 45, no. 3, pp. 909–919, 1999.
[34] F. Nielsen, "Closed-form information-theoretic divergences for statistical mixtures," in *Proc. IEEE Int. Conf. Pattern Recognition*, 2012, pp. 1723–1726.
[35] D. D.-Y. Po and M. Do, "Directional multiscale modelling of images using the contourlet transform," *IEEE Trans. Image Process.*, vol. 15, no. 6, pp. 1610–1620, 2006.
[36] H. Qu and Y. Peng, "Texture image retrieval based on contourlet coefficient modeling with generalized Gaussian distribution," *LNCS 4683*, pp. 493–502, 2007.
[37] T. Randen and J.-H. Husoy, "Filtering for texture classification: A comparative study," *IEEE Trans. Pattern Anal. Mach. Intell.*, vol. 21, no. 4, pp. 291–310, 1999.
[38] C. Robert and G. Casella, *Monte Carlo Statistical Methods*. New York, NY, USA: Springer, 2010.
[39] O. G. Sezer, A. Ertuzun, and A. Ercil, "Using perceptual relation of regularity and anisotropy in the texture with independent component model for defect detection," *Pattern Recognit.*, vol. 40, no. 1, pp. 121–133, 2007.
[40] "Terravic research facial IR database," [Online]. Available: http://www.terravic.com/research/facial.htm 2013
[41] "TILDA textile texture database," [Online]. Available: http://lmb.informatik.uni-freiburg.de/resources/datasets/tilda.en.html 2013
[42] C. S. Wallace, *Statistical and Inductive Inference by Minimum Message Length*. New York, NY, USA: Inf. Sci. & Statist., Springer, 2005.
[43] P. J. Phillips, C. Jiang, and S. Wiener, "Comparison of visible and infrared imagery for face recognition," in *Proc. Int. Conf. Automatic Face and Gesture Recognition*, 1996, pp. 182–187.
[44] Z. Yifan and X. Liangzheng, "Contourlet-based feature extraction on texture images," in *Proc. Int. Conf. Computer Science and Software Engineering*, 2008, pp. 221–224.
[45] W. Zhao, R. Chellappa, P. J. Phillips, and A. Rosenfeld, "Face recognition: A literature survey," *ACM Comput. Surveys*, vol. 35, no. 4, pp. 399–458, 2003.

Mohand Saïd Allili received his MSc and PhD degrees in computer science from the University of Sherbrooke, Quebec, Canada, in 2004 and 2008, respectively. Since June 2008, he has been a Professor of computer science in the Department of Computer Science and Engineering at the University of Quebec in Outaouais (UQO) in Canada. He received the best PhD thesis award in engineering and natural sciences from the University of Sherbrooke for the year 2008. Two of his papers have received best student paper and best vision paper awards at the conferences CRV 2007 and CRV 2010, respectively. His main research interests include computer vision and graphics, image processing, pattern recognition and machine learning.

Nadia Baaziz received the PhD degree in signal processing and telecommunications in 1991 from IRISA, Rennes I University, Rennes, France. From 1992 to 1995, she was a postdoctoral and an associate researcher at the INRS-telecommunications center in Montreal, Canada. She is currently a Professor at the University of Quebec in Outaouais, Gatineau, Canada.

Her teaching and research interests are in the area of signal, image and video processing. Research topics include multi-resolution transforms, coding and image watermarking and retrieval. She is a member of Quebec engineer association OIQ, Canadian Engineering Accreditation Board and IEEE Signal Processing Society.

Marouene Mejri received his MSc degree in Computer Engineering from the École Supérieure des Sciences et Techniques of Tunis (Tunisia), in 2009 and his MSc degree in Computer Science from the University of Quebec in Outaouais, Gatineau, Canada, in 2013. His research interests include image processing, pattern recognition and machine learning.